



## Technical Note

# Electromagnetic Signal Attenuation Characteristics in the Lunar Regolith Observed by the Lunar Regolith Penetrating Radar (LRPR) Onboard the Chang'E-5 Lander

Chunyu Ding <sup>1,2</sup> , Yan Su <sup>3,4,\*</sup> , Zhonghan Lei <sup>1</sup>, Zongyu Zhang <sup>3,4</sup> , Mi Song <sup>2,5</sup>, Yuanzhou Liu <sup>2,5</sup>, Ruigang Wang <sup>6</sup> , Qingquan Li <sup>2,5</sup>, Chunlai Li <sup>3,4</sup> and Shaopeng Huang <sup>2,5,\*</sup>

<sup>1</sup> Institute of Advance Study, Shenzhen University, Shenzhen 518060, China

<sup>2</sup> Space and Earth Interdisciplinary Center, Shenzhen University, Shenzhen 518060, China

<sup>3</sup> Key Laboratory of Lunar and Deep Space Exploration, National Astronomical Observatories, Chinese Academy of Sciences, Beijing 100012, China

<sup>4</sup> School of Astronomy and Space Science, University of Chinese Academy of Sciences, Beijing 100049, China

<sup>5</sup> College of Civil and Transportation Engineering, Shenzhen University, Shenzhen 518060, China

<sup>6</sup> The 54th Research Institute of China Electronic Technology Corporation (CETC), Shijiazhuang 050081, China

\* Correspondences: [suyan@bao.ac.cn](mailto:suyan@bao.ac.cn) (Y.S.); [shaopeng@szu.edu.cn](mailto:shaopeng@szu.edu.cn) (S.H.)

**Abstract:** The Chinese Chang'E-5 probe landed in the Mons Rümker of Oceanus Procellarum on the near side of the Moon. The lunar regolith penetrating radar (LRPR) carried by the Chang'E-5 probe allows for the determination of in situ lunar regolith dielectric properties, which are probably related to the age and chemical composition of the regolith. In this paper, we analyze the Chang'E-5 LRPR data with the frequency shift method to estimate the loss tangent of the lunar regolith within a depth of ~2.8 m. The loss tangent of the Chang'E-5 landing site is constrained to be  $0.0148 \pm 0.0016$ , which is substantially higher than that of the typical lunar regolith. The high loss tangent is found to be characteristic of the young basalt age (~2.0 Ga) and high  $\text{TiO}_2 + \text{FeO}$  content ( $28.21 \pm 1.57\%$ ) of the Chang'E-5 landing site. Integrated analysis of results from Chang'E-3, Chang'E-4, and Chang'E-5 show that the younger is the geologic age of the mare unit, the greater is the loss tangent of the lunar regolith, and the weaker is the radar electromagnetic signal penetrating ability.

**Keywords:** China lunar exploration program (CLEP); lunar regolith penetrating radar (LRPR); loss tangent estimation; radar pulse attenuation; frequency shift method



**Citation:** Ding, C.; Su, Y.; Lei, Z.; Zhang, Z.; Song, M.; Liu, Y.; Wang, R.; Li, Q.; Li, C.; Huang, S. Electromagnetic Signal Attenuation Characteristics in the Lunar Regolith Observed by the Lunar Regolith Penetrating Radar (LRPR) Onboard the Chang'E-5 Lander. *Remote Sens.* **2022**, *14*, 5189. <https://doi.org/10.3390/rs14205189>

Academic Editors: Cyril Grima and Long Xiao

Received: 3 August 2022

Accepted: 11 October 2022

Published: 17 October 2022

**Publisher's Note:** MDPI stays neutral with regard to jurisdictional claims in published maps and institutional affiliations.



**Copyright:** © 2022 by the authors. Licensee MDPI, Basel, Switzerland. This article is an open access article distributed under the terms and conditions of the Creative Commons Attribution (CC BY) license (<https://creativecommons.org/licenses/by/4.0/>).

## 1. Introduction

The Moon is the closest neighbor and the only satellite of Earth. It is the preferred target for human beings to explore extraterrestrial objects. Ever since the former Soviet Union launched Luna 2 in September 1959, which landed east of the Mare Tranquillitatis, human beings have carried out numerous exploration missions to the Moon, of which the success rate has been about 50% (Ding et al. [1]). Following China's successful launch of the Chang'E-1 mission in 2007, it has successfully completed five lunar exploration missions and achieved fruitful scientific research results (Li et al. [2]). The Moon's subsurface preserves rich information on various impacts experienced by the Moon during the early formation of the solar system and its later modification (Hörz et al. [3]). Among the important research objects of lunar exploration are radar observation and drilling sampling to the lunar regolith to obtain information. A detailed study of the dielectric properties of the lunar regolith and its formation mechanism can promote interpretation of the formation history and evolution mechanism of the surface of the Moon (Carrier et al. [4]).

In radar observations of the Moon, it is very important to derive the dielectric properties of targets (Campbell and Ulrichs [5], Feng et al. [6], Ding et al. [7], Li et al. [8], Ding et al. [9]). Radar penetration capability mainly depends on the loss tangent of the subsurface material (Pommerol et al. [10], Xing et al. [11]). The optical detection means concerning the Moon

mainly reflect the physical characteristics of materials on the surface (Hillier et al. [12], Sato et al. [13]), while its penetrability is almost negligible relative to the thickness of the lunar regolith. The Chinese Chang'E-3, Chang'E-4, and Chang'E-5 landed on geological units of the lunar surface with different ages, and all carried surface penetration radar (Li et al. [8], Ding et al. [9], Fang et al. [14], Su et al. [15], Xiao et al. [16], Zhou et al. [17], Wang et al. [18]), which provides an unprecedented opportunity to quantify the relationship between the loss tangents and the ages of different geological units.

The dielectric properties of the lunar regolith are mainly characterized by the dielectric permittivity. Generally, the dielectric permittivity is a complex, with its real part being the relative permittivity and the loss tangent provided by the ratio between the imaginary and real parts of the complex permittivity (Ulaby et al. [19], Orosei et al. [20]). The loss tangent is commonly used in planetary radar to denote the attenuation of electromagnetic wave energy by a medium, while conductivity is commonly used in geophysics on Earth. The conductivity and loss tangent indicate a measure of how easily electrical current flows through a material (Carrier et al. [4]). The relative permittivity and loss tangent of the subsurface material can be retrieved from the radar echoes to determine the characteristics of the target material during radar observation of the Moon. For example, the relative permittivity of a typical lunar regolith is  $\sim 3$  and the loss tangent is  $\sim 0.005$  (McKay et al. [21]). Typical lunar basalts have a relative permittivity of 6–12 and loss tangents of  $>10^{-2}$  (McKay et al. [21]). The loss tangents of the lunar regolith have a large range of variation, e.g., the loss tangents of the lunar regolith at the Chang'E-3, Chang'E-4, and Apollo17 landing sites are  $\sim 0.0124$ ,  $\sim 0.005$ , and  $\sim 0.008$ , respectively (Li et al. [8], McKay et al. [21], Ding et al. [22], Strangway et al. [23]). The possible reason for this phenomenon is that there are differences in  $\text{TiO}_2 + \text{FeO}$  content in the lunar regolith and/or the age of geological units of the Moon's surface. However, there have been no reports on how to quantify the relationship between the loss tangent and the age of the Moon's surface. Although the loss tangent of the Chang'E-5 lunar regolith is estimated using the method of amplitude attenuation of the radar echo (Su et al. [15]), the amplitude of radar echo is commonly affected by multiple reflections, geometric spreading, and scattering, which make challenging to obtain reliable attenuation (Liu et al. [24]). However, the frequency shift method can effectively avoid the influence of this situation (Ding et al. [22], Liu et al. [24], Irving and Knight [25]).

In this paper, the loss tangent in the lunar regolith of the Chang'E-5 landing site is estimated using the frequency shift method and the relationship between the loss tangent in the lunar regolith and the age of the Moon's surface is quantitatively derived. This empirical relationship provides a reference for estimating the penetration depth of the Moon's surface with different ages observed by radar.

## 2. Geological Background, Data Collection, and Method

### 2.1. Geological Background of the Chang'E-5 Landing Site

In 2020, China launched the Chang'E-5 mission, which is the "return" stage in the trilogy of "orbiting, landing, and return" of China's Lunar Exploration Program (CLEP). Lunar samples totaling  $\sim 1731$  g were collected by the mechanical arm and core drilling sampling on the lander and returned to Earth (Li et al. [26]). The landing site of the Chang'E-5 mission is located on the Eratosthenian-aged mare basalt in the Mons Rümker of Oceanus Procellarum (Qiao et al. [27]), and its geological age of the local mare unit is constrained to  $\sim 2.0$  Ga (Li et al. [28], Che et al. [29]). The topography of the landing site is relatively flat, with an average slope of  $2.7^\circ$  (Wu et al. [30]).

The Xu Guangqi crater is located to the northwest of the lander (Figure 1A), and has a diameter of  $\sim 463$  m. Combined with the distribution of the surrounding craters and the geological background of the landing site, the Xu Guangqi crater is considered as a primary impact crater formed before 400 Ma (Qiao et al. [27], Su et al. [31]). The mixed thickness of the indigent lunar regolith and ejecta materials over the bedrock in the landing site is constrained to  $\sim 7$  m (Qian et al. [32]). The survey line of the LRPR is located at the distal of the continuous ejecta of the Xu Guangqi crater (Figure 1C). According to impact crater theory (McGetchin et al. [33], Pike [34]), the thickness of the Xu Guangqi crater's ejecta deposited at the landing site yielded  $\sim 0.6$  m (see Table 1 for details). In addition, there is a crater, named Crater A, with a diameter of  $\sim 104$  m in the southeast of the Xu Guangqi crater. Crater A was formed later than 400 Ma, as it is located on the continuous ejecta blanket of the Xu Guangqi crater. Because of its relatively small diameter, Crater A was not excavated deeply enough to reach the underlying bedrock, and as such its ejecta materials are mainly sourced from the ejecta of the Xu Guangqi crater and the paleo-regolith. The contribution of the deposited materials of Crater A to the landing site is  $\sim 0.2$  m (see Table 1). According to the image data acquired by the Chang'E-5 high-resolution landing camera (Figure 1B), there are three small craters near the lander which have diameters of 11.12 m (Crater C1), 7.82 m (Crater C2), and 7.30 m (Crater C3). The contributions of the ejecta from these three craters to the landing site are small, indeed negligible (see Table 1). Therefore, the materials with a depth of 1 m below the lunar surface of the Chang'E-5 landing site are possibly from the sum of the Xu Guangqi crater and Crater A. These ejecta materials have undergone weathering on the lunar surface for less than 400 Ma, and are mainly dominated by the lunar regolith, with a small amount of rock fragments (Su et al. [31], Feng et al. [35]).

**Table 1.** The size information of the Xu Guangqi, A, C1, C2, and C3 craters.

Crater	Diameter (m)	Depth (m)	Distance to the Lander (m)	Ejecta Deposits to the CE-5 Site (m)
Xu Guangqi	463	66	424	0.590–0.638
A	104	7	91	0.152–0.242
C1	11.12	1.38	14.35	0.005–0.144
C2	7.82	0.91	17.69	0.0007–0.002
C3	7.30	1.18	14.68	0.0009–0.003

Note: The ejecta thickness estimation at the CE-5 landing site are calculated based on the McGetchin et al. [33], and Pike [34] models, respectively.

## 2.2. Data Collection and LRPR Description

The Chang'E-5 LRPR consists of lunar surface array antenna penetrating radar equipment with a central frequency of 2 GHz and a bandwidth of 1–3 GHz (Xiao et al. [16]); its vertical resolution in lunar regolith-like material is designed to be 5 cm (Li et al. [36], Xiao et al. [16]). Unlike the radar systems installed on the Chang'E-3 and Chang'E-4 rovers, it can detect radio signals while traveling (Fang et al. [14], Su et al. [15]). The Chang'E-5 LRPR is installed at the bottom of the lander and cannot be moved for detection (Figure 2A). It consists of twelve antenna pieces, marked #1 to #12 (red rectangle in Figure 2A); the spacing between the antennas is 0.12 m, and the length of the horizontal survey line is fixed at 1.56 m (Xiao et al. [16], Su et al. [31]). Its working principle is that the first antenna emits electromagnetic waves into the lunar surface; the other eleven receive the reflected echoes, then loop to the next piece of antenna for transmission while the other antennas receive signals. This loop repeats until reaching the final antenna piece. Therefore, the LRPR can obtain 132 radar data traces in a completed observation.

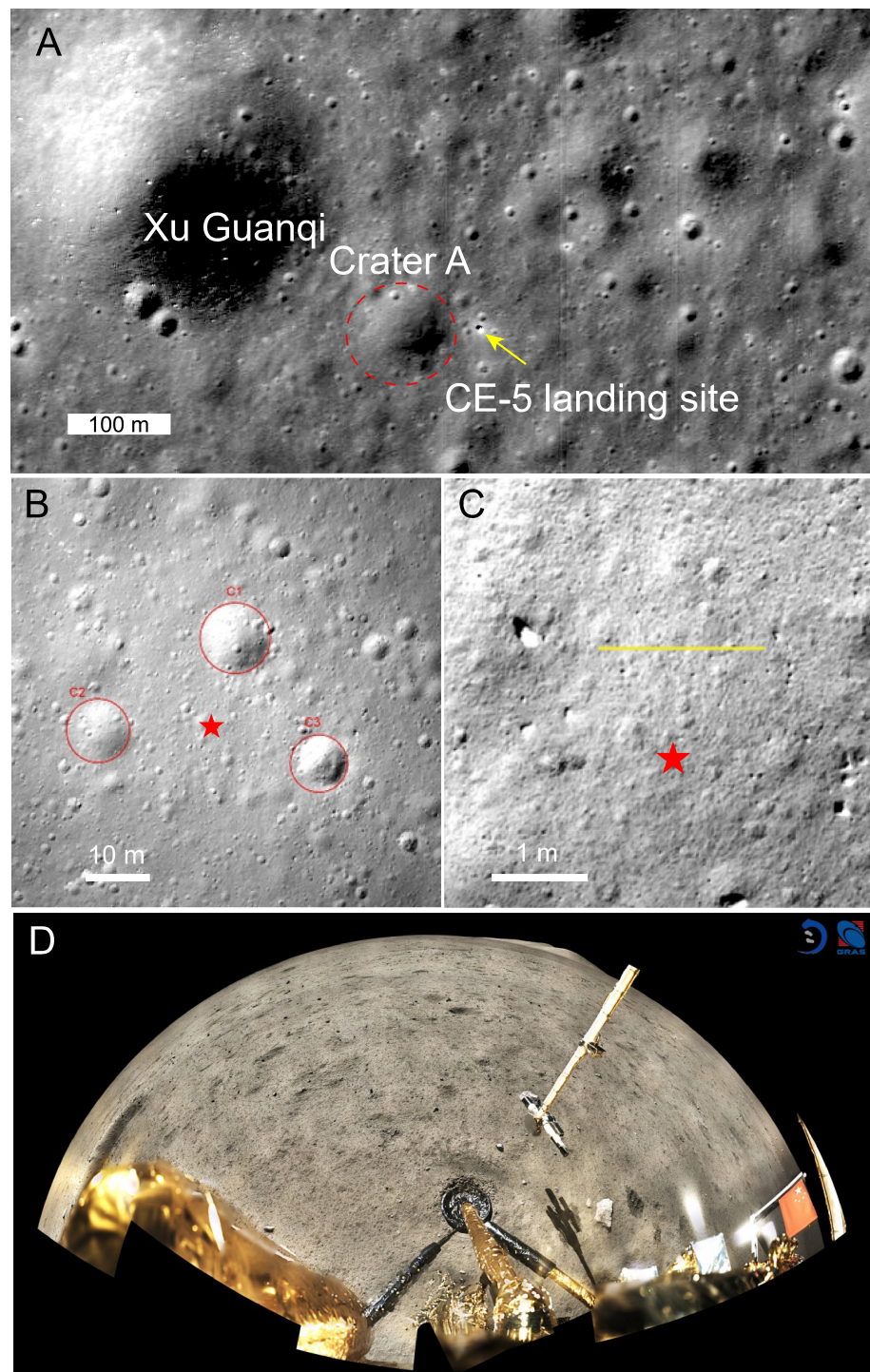


**Figure 1.** Geological background of Chang'E-5 landing site. (A) The Chang'E-5 lander is located on the Eratosthenian-aged mare basalt on the near side of the Moon. The dashed red circle indicates the position of Crater A, which has a diameter of  $\sim 104$  m and a depth of  $\sim 7$  m (Su et al. [31]). The base image is from LROC NAC data with a resolution of 1.5 m/pixel (Image ID:M1361560086RE). (B) The lander is surrounded by three small craters (C1, C2, and C3); the base image was acquired by Chang'E-5 landing camera, which has a resolution of 5 cm/pixel. (C) The yellow line represents the LRPR survey line, and is approximately 1.56 m. The red star indicates the position of the lander. The base image is from the Chang'E-5 landing camera, which has a resolution of 1 cm/pixel. (D) Image of the lunar surface acquired by the lander camera; the image shows the distribution of a small amount of rock fragments. The images acquired by Chang'E-5 can be freely download from <https://moon.bao.ac.cn/ce5web/moonGisMap.search>, accessed on 2 August 2022.

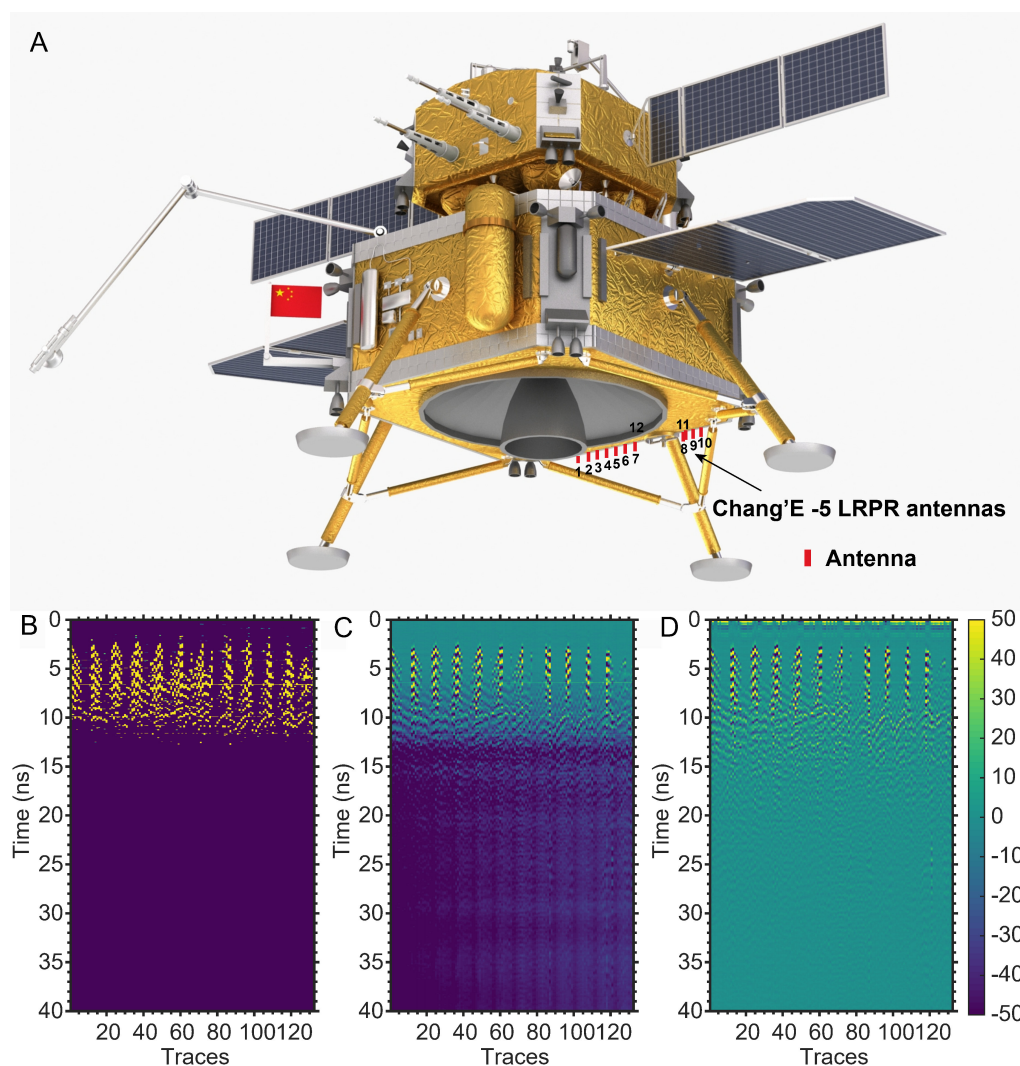


**Figure 2.** The model and LRP observation data from Chang'E-5. (A) The module model of the Chang'E-5 lander; the LRPR is installed at the bottom of the lander ([www.turbosquid.com/zh\\_cn/3d-models/chang-e-5-e-model-1681820](http://www.turbosquid.com/zh_cn/3d-models/chang-e-5-e-model-1681820), accessed on 2 August 2022). (B) Raw radar data. (C) Radar data after system gain removal and sampling calibration. (D) Radargram after band-pass filtering (1–3 GHz).

During the ground verification test, it was found that the lander body wrapped in metal interfered with the subsurface echo (Xiao et al. [16], Li et al. [36], Feng et al. [37]). During the trip to the Moon, the LRPR observed the universe three times (Su et al. [31]). These three sets of data are mainly used to deduct the background interference of the lander body in the measured data. Before drilling a sampling of the lunar regolith, the LRP was turned on to detect one set of data, which was used to guide and assist core drilling sampling. After the core drilling was completed, three groups of observation data were obtained, for a total of seven groups of datasets.

For the purpose of estimating the loss tangent of the lunar regolith, we use only the radar data before drilling, as the metal casing of the drilling core remains in the lunar regolith after drilling, which may affect the final results. The data used in this paper are the raw data issued by the Ground Application System of CLEP of National Astronomical Observatory, Chinese Academy of Sciences. The raw radar data are displayed in Figure 2B. In order to improve the signal-to-noise ratio of the data, we introduced routine approaches for preprocessing of radar data, e.g., system gain removal and sampling calibration (Figure 2C) and band-pass filtering (Figure 2D). The system gain removal is

different from those of the Chang'E-3 and Chang'E-4 radars' data. There are 132 data traces stored in a file of the LRPR, in which each trace has 3000 time sampling points with a time interval of 0.018315 ns; thus, the corresponding radar echo time window is  $\sim 55$  ns. These 132 data traces use the same time-variable gain, and the parameters of the gain are stored in the header file of each dataset, which consists of bytes 71 to 310. The first 240 sampling points correspond to 240 gain values, and the rest of the sampling points correspond to the last gain value. The relationship between the gain parameter ( $G_{para}$ ) and the gain value ( $G_{value}$ ) is expressed as  $G_{value} = -G_{para}/2$ . The original voltage ( $V_{raw}$ ) of the LRPR signal can be converted using the following equation:

$$G_{value} = 20 * \log_{10}\left(\frac{V_{ob}}{V_{raw}}\right) \quad (1)$$

where  $V_{ob}$  is the measured voltage of the LRPR observation, which is the data after system gain removal.

The LRPR antennas are approximately 0.9 m away from the Moon's surface (Xiao et al. [16]), and radar echoes received by the each antenna have a different time delay from the ground surface. To estimate the loss tangent of the lunar regolith using the LRPR data, we do not calculate the radar echo between the antennas and the lunar surface; thus, we need to obtain the accurate position of the zero point of the lunar surface. By comparing the geometrical relationship between the spacing of antennas and its height away from the lunar surface, we obtained the time delay of the zero point, which ranges from  $\sim 5.9$  ns to  $\sim 11.9$  ns, as shown in Figure 3.

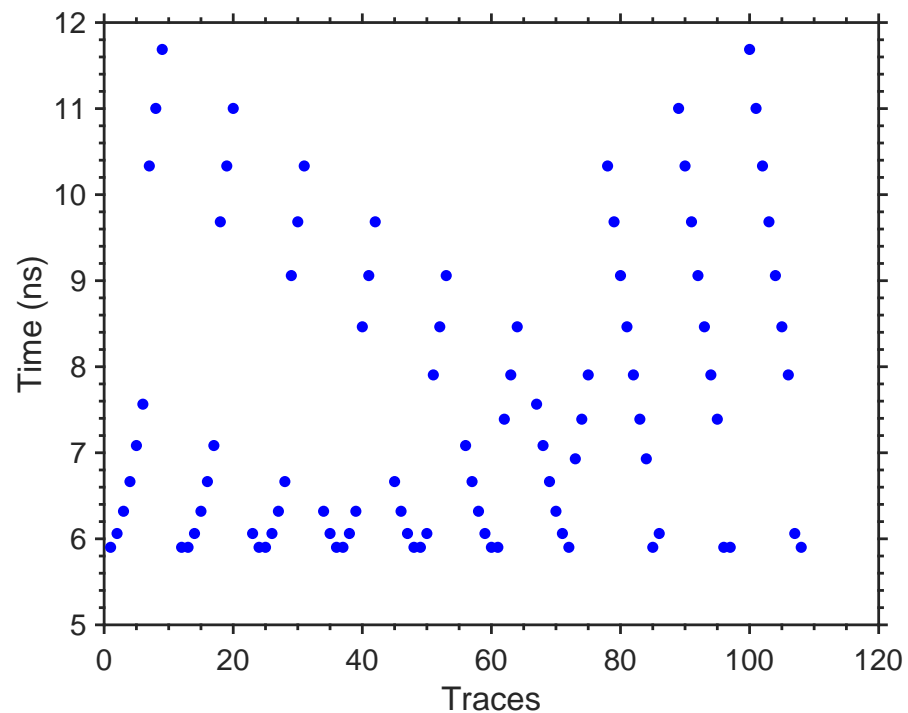


**Figure 3.** Zero points of the lunar surface calculated by the radar echoes received by the antennas #1 to #10. The blue dots represent the two-traveling time delay of the lunar ground surface reflector of the radar echoes received by the antennas.

### 2.3. Frequency Shift Method

While LRPR-emitted radar electromagnetic waves propagate in a lossy medium, the centroid frequency of the echo signal is broadened with time. This phenomenon is called frequency shift (Liu et al. [24], Quan and Harris [38]). Based on the frequency shift method, the attenuation rate of a radar electromagnetic wave propagating in a lossy

medium can be estimated and the loss tangent of the lossy medium can be derived (Irving and Knight [25]). This method has been successfully applied to the inversion of dielectric properties of volcanic ash (Lauro et al. [39]) and lunar regolith observations by lunar penetrating radar (Ding et al. [22]).

There is a linear relationship between the centroid frequency of radar echo signals, the centroid frequency of radar transmitting antennas, and the loss tangent of the medium in which it propagates (Equation (2)). The detailed derivation process can be found in our previous study (Ding et al. [22])

$$f_r = f_t - \frac{\pi \cdot \tan \delta \cdot f_t}{8} \tau \quad (2)$$

where  $f_r$  is the centroid frequency of the signal received by the radar antenna;  $f_t$  is the centroid frequency of the radar transmitting antenna, which is approximately equivalent to the operating frequency of the radar (Quan and Harris [38]);  $\tan \delta$  is the loss tangent of the propagation medium; and  $\tau$  is the two-way traveling time (ns). The centroid frequency  $f_r$  of the signal received by the radar antenna can be calculated using

$$f_r = \frac{\int_0^\infty f \cdot Y(f) df}{\int_0^\infty Y(f) df} \quad (3)$$

where  $Y(f)$  is the spectrum of the signal received by the radar antenna. By fitting the trend of the centroid frequency of the radar echo signal to the time using Equation (2), the frequency shift rate of radar electromagnetic wave propagation in a lossy medium can be obtained. The loss tangent can subsequently be calculated by (Quan and Harris [38])

$$\tan \delta = -8 \left( \frac{\Delta f_r}{\Delta t} \right) / \left( \pi \cdot f_t^2 \right) \quad (4)$$

where  $\frac{\Delta f_r}{\Delta t}$  is the slope of the frequency downshift varying with time.

### 3. Results

#### 3.1. Loss Tangent Estimation

The time window of LRPR is  $\sim 55$  ns, and the zero points to the lunar surface range from  $\sim 6$  ns to  $\sim 12$  ns (Figure 3). In the ground verification experiment, the earth's volcanic ash is treated as the simulant of the lunar regolith. The data obtained by the LRPR from the regolith simulant show that there is a group of strong reflections at the end of the signal and that its peak value is  $\sim 54.4$  ns (Figure 4C,D). This reflected signal is not from the subsurface materials; rather, it is from the reflection of the cable in the radar system, which is an artificial signal. Similarly, there is a group of strong reflections at the end of the signal in the lunar observation data, with a peak value of  $\sim 52.4$  ns (Figure 4A,B). However, the range of the strong reflections from the radar observation of the lunar regolith is wider than that from the ground experiment, which is from  $\sim 44.5$  ns to  $\sim 52.9$  ns. While the subsurface reflections of the lunar regolith range from the zero point of the lunar surface to  $\sim 44.5$  ns, the amplitude of the radar echo is attenuated with time, which accords with the characteristics of electromagnetic signal propagation in the lunar regolith. However, it sharply rises at  $\sim 44.5$  ns, which may be due to an interface between different dielectric properties, such as rocks or mare basalt, although Qian et al. [32] concluded that as the thickness of the lunar regolith at the Chang'E-5 landing site is  $\sim 7$  m, it is most likely due to rocks. The strong reflection signal at  $\sim 44.5$  ns cannot be well distinguished from the system cable reflection. Therefore, in order to avoid ambiguity, we chose the signal before  $\sim 44.5$  ns for use in this study.

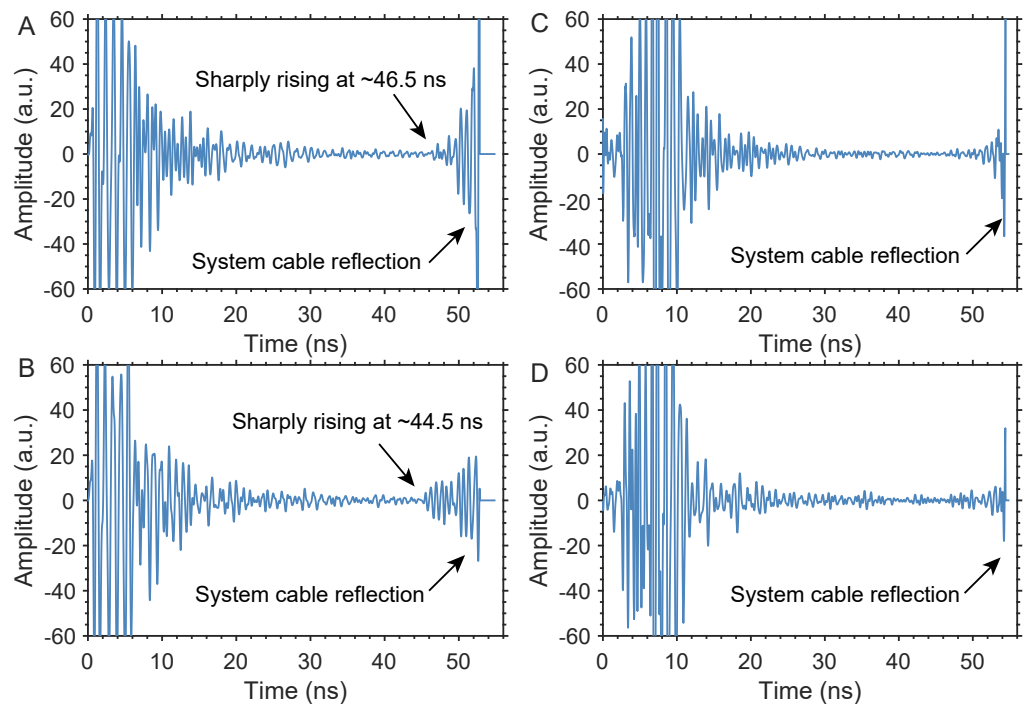


**Figure 4.** Comparative analysis of the lunar observation data (A,B) and ground verification data (C,D) obtained by the LRPR and LRPR prototype. In the ground verification experiment, the lunar regolith simulant observed by the LRPR is made of terrestrial volcanic ash. Here, the radar signals are received by the closest spacing between the transmitting antenna and the receiving antenna.

In calculating the loss tangent, we have subtracted the radar echoes from the antennas to the lunar surface, which propagate in a vacuum. Because the height of the antennas to the lunar surface is  $\sim 0.9$  m, the radar coupling wave and the direct wave have separated and are prior to the zero point of the lunar surface. Therefore, in order to avoid the influence of the coupling wave and other clutter on our calculation results, we choose the radar echoes after the zero point of the lunar surface, e.g.,  $\sim 12$  ns. First, every trace of the radar echo is transformed by short-time Fourier transform and the time-frequency distribution is obtained. Second, the centroid frequency of the radar echo at each time is calculated using Equation (3) and the plots of time various with centroid frequency is obtained. Third, the time-frequency distribution data are fitted in order to obtain the frequency shift rate. Finally, the loss tangent in the lunar regolith can be obtained by substituting the calculated frequency shift rate into Equation (4).

Radar antennas #1 to #12 transmit electromagnetic wave pulses in turn, and other antennas receive echo signals, receiving 132 data traces in total. Taking the transmitting antenna as the division, the centroid frequencies of twelve groups of radar echo signals and their change over time are shown in Figure 5A–L. Among them, the transmission frequency  $f_t$  is set to the operation frequency of the LRPR with 2 GHz, and only the frequency shift rate is an unknown parameter in the fitting equation (Equation (2)). The radar echo signals of each group of antennas in Figure 5 are calculated using the fitting method, with the obtained parameters shown in Table 2.

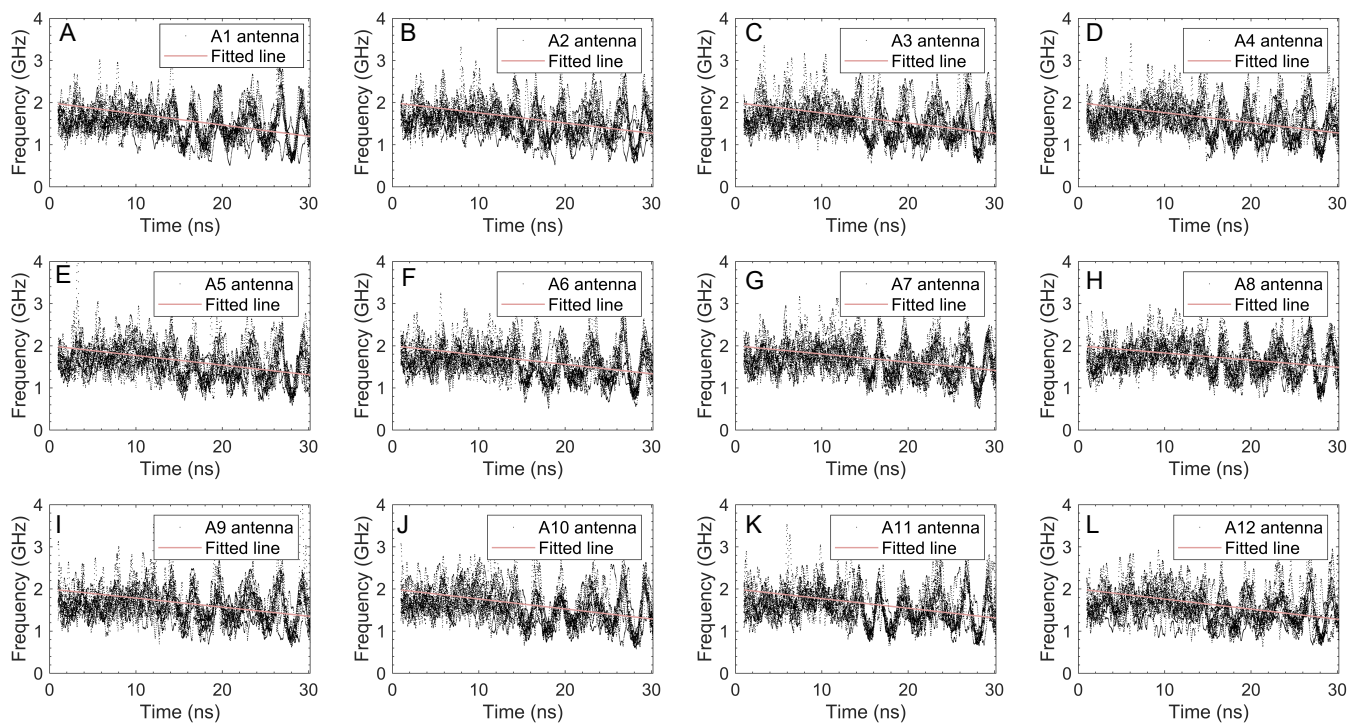


**Figure 5.** The centroid frequency of the radar echo versus time. (A–L) are the centroid frequencies of radar echoes obtained by antennas #1 to #12 as transmitting antennas and other antennas as receiving antennas, respectively. The horizontal axis is the two-way traveling time (ns) and the vertical axis is the centroid frequency (GHz). The pink line is the best fitting result. It is worth noting that we use the data prior to band-pass filtering to calculate the frequency shift rate.

**Table 2.** Parameters of the best fitting lines and their 95% confidence intervals.

Antenna	Slope, Frequency Shift Rate (GHz/ns)	95% Confidence Interval
#1	0.0266	(0.0262, 0.0269)
#2	0.0242	(0.0239, 0.0246)
#3	0.0243	(0.0239, 0.0246)
#4	0.0239	(0.0236, 0.0242)
#5	0.0229	(0.0226, 0.0232)
#6	0.0221	(0.0218, 0.0224)
#7	0.0194	(0.0191, 0.0197)
#8	0.0170	(0.0167, 0.0173)
#9	0.0215	(0.0211, 0.0218)
#10	0.0236	(0.0233, 0.0240)
#11	0.0228	(0.0225, 0.0232)
#12	0.0239	(0.0235, 0.0242)

The median frequency shift rate of the LRPR radar wave within a depth of  $\sim 2.8$  m below the lunar surface is  $0.0233 \pm 0.0025$  GHz/ns; the relative permittivity is assumed to be  $\sim 3.04$ , which is obtained by the Chang'E-5 regolith laboratory measurement (see Su et al. [31]). By substituting the frequency shift rate in Table 2 into Equation (4), the value of the loss tangent retrieved from the radar echo signals of each group of antennas can be obtained. The median value of the loss tangent within the lunar regolith calculated by frequency shift method is 0.0148, and its  $1\delta$  standard deviation is 0.0016 (Figure 6) for the Chang'E-5 landing site.

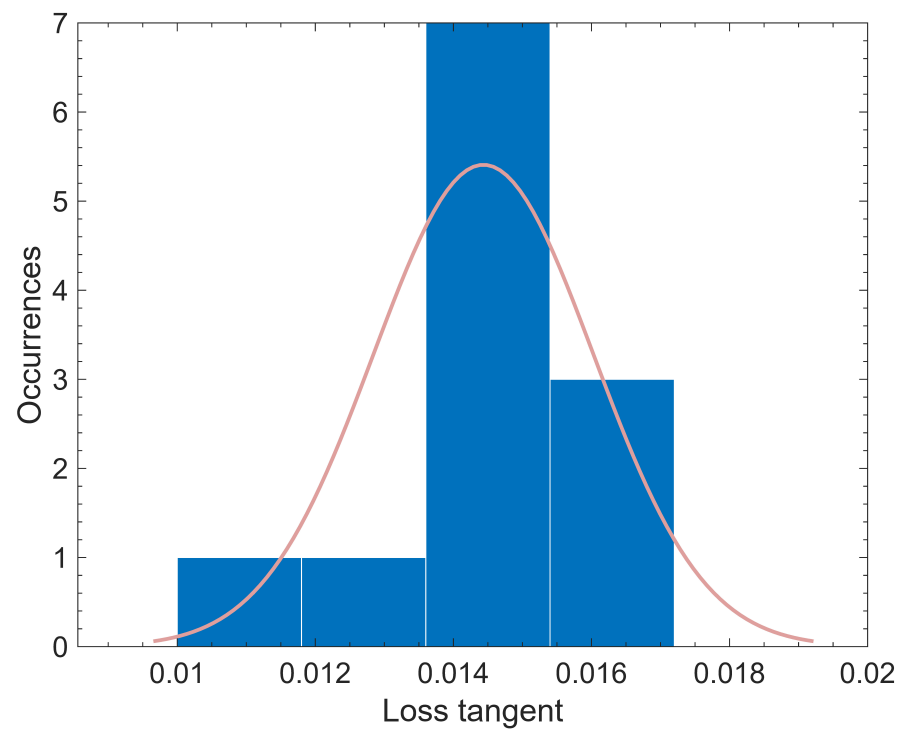


**Figure 6.** Histogram of the calculated loss tangent in the lunar regolith at the Chang'E-5 landing site.

### 3.2. $TiO_2+FeO$ Content Estimation

Laboratory measurement results of Apollo samples show that the loss tangent of lunar samples is related to their density and chemical characteristics, especially their  $TiO_2+FeO$  content. In this paper, we only considered the case of the lunar regolith; thus, the empirical formula is adopted by only fitting the results of Apollo lunar regolith samples (Carrier et al. [4]), exhibited as

$$\tan\delta = 10^{0.030 \times (TiO_2+FeO)\% - 2.676} \quad (5)$$

where  $\tan\delta$  is the loss tangent of the lunar regolith and  $TiO_2+FeO$  is the content of ferrotitanium in the lunar regolith. By substituting the loss tangent estimated in Section 3.1 into Equation (5), the  $TiO_2+FeO$  content in the lunar regolith at the Chang'E-5 landing site is found to be  $28.21 \pm 1.57\%$ .

## 4. Discussion

### 4.1. Relationship between the Loss Tangent and the Moon's Surface Age

The Chinese Chang'E-3 mission landed on the eastern rim of the Ziwei crater, and the survey line detected by Yutu radar was on the continuous ejecta blanket of the Ziwei crater (Xiao et al. [40]). The theoretical deposited thickness of the ejecta material excavated in the Ziwei crater at the landing site is constrained to  $\sim 5$  m (Qiao et al. [41]), and the formation age of the Ziwei crater is constrained to  $\sim 26.7$  Ma (Xiao et al. [40]). This indicates that the materials within a thickness of  $\sim 5$  m at the Chang'E-3 landing site may be ejecta materials formed by the Ziwei crater. However, it remains to be clarified whether these ejecta materials are mainly the lunar regolith or underlying broken basalt fragments. According to impact theory, the excavation depth of a crater is about 1/13 of its diameter (Melosh [42]). As the diameter of Ziwei crater is  $\sim 450$  m, the excavation depth of the crater is  $\sim 34.62$  m. Quantitative analysis of the percentage of the lunar regolith in a given crater's ejecta can be estimated using the following equation (Taylor et al. [43]):

$$P = \frac{100T}{D_E \times d} \quad (6)$$

where  $P$  is the percentage of the lunar regolith;  $T$  is the thickness (m) of the in situ lunar regolith before excavation;  $D_E$  is the coefficient of the excavation depth and crater depth, which is in the range of 0.2–0.3 based on laboratory simulations of crater data (Stöffler et al. [44]); and  $d$  is the depth of crater (m). It is worth noting that the product of  $D_E$  and  $d$  is the maximum excavation depth of the crater (Taylor et al. [43]). The average lunar regolith thickness before excavation at the Chang'E-3 landing site is  $\sim 8$  m (Fa et al. [45]). According to Equation (6), the percentage of lunar regolith in the ejecta of Ziwei is  $\sim 23.11\%$ ; thus, it can be inferred that most of the ejecta originates from the broken underlying basalt. However, the relative permittivity within  $\sim 4$  m below the lunar surface yields  $\sim 3.2$  (Ding et al. [46], Fa et al. [47]), suggesting that the Ziwei ejecta are similar to that of the lunar regolith. Other scholars believe that the ejecta volume and excavation depth of a crater may be 3–4 times less than the previous estimates (Sharpton [48]), meaning that the percentage of the lunar regolith in the Ziwei ejecta can be recalculated as 69.32–92.43%, which is consistent with the radar observations. Therefore, it is highly possible that the Ziwei ejecta are mainly local material developed on the Eratosthenian-aged mare basalt, with an age of  $\sim 2.5$  Ga (Xiao et al. [40]) and a loss tangent of  $0.0124 \pm 0.0023$  (Ding et al. [22]), as marked by the yellow dot in Figure 7.

The Chinese Chang'E-4 mission landed at the bottom of Von Kármán crater at  $\sim 3.6$ – $3.7$  Ga on the far side of the Moon (Chang et al. [49], Huang et al. [50], Pasckert et al. [51]). The observation results from its high-frequency radar show that the material  $<45$  m below the lunar surface are ejecta materials from the Orientale basin (Xiao et al. [52]), while the shallow surface layer on the top, which is  $\sim 12$  m thick, is fine-grained lunar regolith with a loss tangent constraint of  $0.005 \pm 0.002$  (Li et al. [8]), as marked by the red dot in Figure 5. The age of the Chang'E-5 landing site has been measured at  $\sim 2.0$  Ga as derived from isotopic measurements (Li et al. [28]).

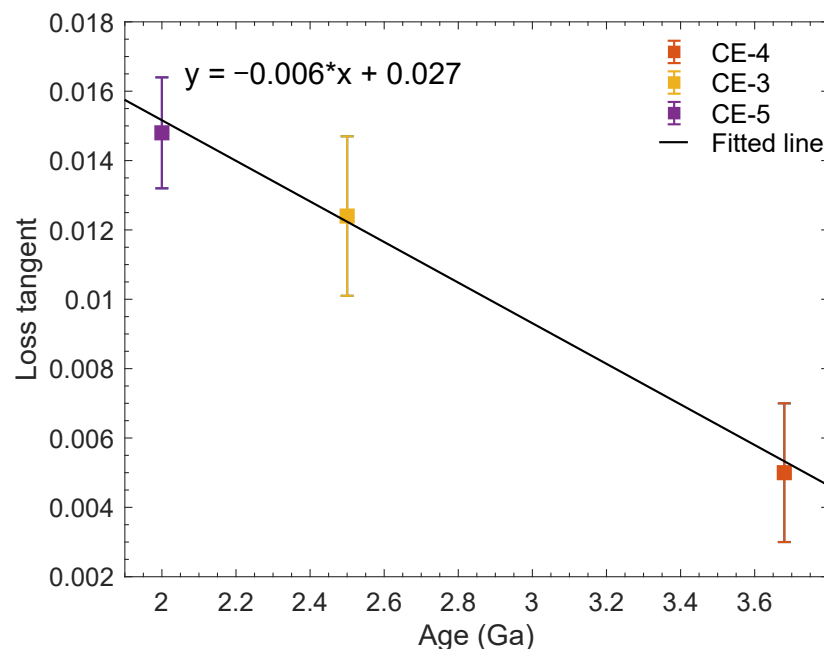


**Figure 7.** The relationship between the Moon's surface age and the loss tangents obtained by the Chang'E-3 (Ding et al. [22]), Chang'E-4 (Li et al. [8]), and Chang'E-5 radars.

The complex permittivity of the lunar regolith simulant sample at different frequencies was tested by Boivin et al. [53], suggesting that the loss tangent has a slight frequency dependence. An assumption for the comparison of the results in Figure 7 is that the dependence of the loss tangent on the frequency relative to the uncertainty of its estimated value can be ignored. To sum up, the loss tangent and geological age of the Chang'E-3, Chang'E-4, and Chang'E-5 landing areas are plotted in Figure 7. Because it is difficult to

unify the geological age deviation value of the landing area of each mission, we adopt the approximate values here. Based on the fitting method, the empirical formulas for obtaining the loss tangent in different geological ages is as follows:

$$y = -0.006x + 0.027; R^2 = 0.98 \quad (7)$$

where  $y$  is the loss tangent of the lunar regolith and  $x$  is the geological age (Ga) of the Moon's surface. It can be inferred that if the geological age is older, the loss tangent in the lunar regolith is smaller. Meanwhile, an older lunar surface age indicates high self-similarity of the materials inside the lunar regolith (Ding et al. [54]). It should be noted that in this paper the geological age of the Moon's surface is the age of the local mare unit. If the lunar regolith is developed on the ejecta materials rather than local bedrock, the source of the ejecta materials need to be determined. In general, crater ejecta are due to the excavation of local materials, with the impact process being one of the physical processes that promote the development of the lunar regolith. It is important to be clear that if the ejecta are excavated locally, the surface age is the local mare basalt. In the case of lunar regolith developed from foreign ejecta materials, the formed age of the parent crater and/or basin should be determined.

#### 4.2. Comparison of Estimated Loss Tangent with Apollo Data

The value of loss tangent in the Chang'E-5 lunar regolith is obviously higher than that of the typical lunar regolith, although it is close to that of the lunar basalt. A possible reason for this is that the geological age of the Chang'E-5 landing area is relatively young, and the  $\text{TiO}_2+\text{FeO}$  content in the lunar regolith is relatively high. Laboratory measurement of Apollo samples shows that the range of the loss tangent of the lunar regolith fluctuates greatly, and is related to the  $\text{TiO}_2+\text{FeO}$  content (Carrier et al. [4]). Figure 8 shows the loss tangent and  $\text{TiO}_2+\text{FeO}$  content in the lunar regolith retrieved by Chang'E-3 (Ding et al. [22]), Chang'E-4 (Li et al. [8]), and Chang'E-5 radars compared to the results from Apollo samples (Carrier et al. [4]). It can be found that the values from Chang'E radar sounding in the lunar regolith are within the measured laboratory values of the Apollo lunar regolith samples. The loss tangent of the Chang'E-5 lunar regolith is greater, which indicates that the  $\text{TiO}_2+\text{FeO}$  content of the lunar regolith at the landing site is higher.

When a radar's electromagnetic wave propagates in a region with higher  $\text{TiO}_2+\text{FeO}$  content, more energy is absorbed, leading to weaker penetration depth (Pommerol et al. [10]). The estimated  $\text{TiO}_2+\text{FeO}$  content at the Chang'E-5 lunar regolith is  $28.21 \pm 1.57\%$ , which is consistent with the actual laboratory measured  $\text{TiO}_2+\text{FeO}$  content in lunar regolith samples ( $\sim 27.5\%$ , per Su et al. [31]) and slightly lower than the  $\text{TiO}_2+\text{FeO}$  content in the landing area observed by the Kaguya Multiband Imager  $\sim 22.9\%$  (Qian et al. [32]). A possible reason for this is that the Kaguya Multiband Imager is a space-borne observation platform with a spatial resolution  $>20$  m/pixel (Lemelin et al. [55]), and does not have the ability to penetrate the lunar regolith. Therefore, it is reasonable for there to be differences between in situ and remote sensing observations.

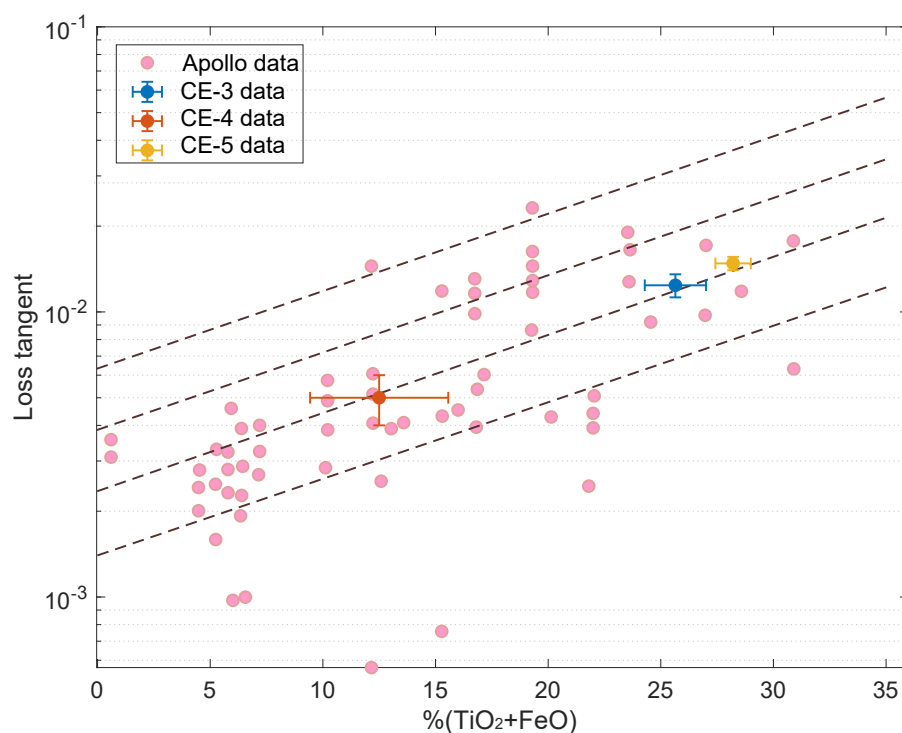


**Figure 8.** Relationship between the loss tangent and ferrotitanium content ( $\text{TiO}_2+\text{FeO}$ ). The pink dots represent laboratory measurements of Apollo lunar regolith samples (Carrier et al. [4]), while green, red, and yellow represent the results of the loss tangents derived from Chang'E-3, Chang'E-4, and Chang'E-5 radar data, respectively.

#### 4.3. The Influence of $\text{TiO}_2+\text{FeO}$ Content in the Lunar Regolith on the Loss Tangent

Generally, the loss tangent in the lunar regolith is associated with the attenuation rate of the electromagnetic signal, which affects the penetrating depth of the radar, and the loss tangent is determined by the  $\text{FeO}+\text{TiO}_2$  content in the lunar regolith (Pommerol et al. [10], McKay et al. [21]). The loss tangent of the Chang'E-5 regolith is  $\sim 0.0148$ , constrained by the LRPR, and its  $\text{TiO}_2+\text{FeO}$  content is derived as  $\sim 28.21$  wt.% using the empirical formula. Laboratory measurements of the Chang'E-5 lunar regolith samples show that the contents of  $\text{FeO}$  and  $\text{TiO}_2$  are 22.2 wt.% and 5.7%, respectively (Tian et al. [56]), which are consistent with our radar observations. In addition, Fa and Wieczorek [57] concluded that the loss tangent of the lunar regolith is more closely related to its  $\text{TiO}_2$  content than its  $\text{FeO}$  content. According to the empirical formula provided in Fa and Wieczorek [57], the  $\text{TiO}_2$  content of the lunar regolith is derived as  $\sim 8.13$ %, which is slightly higher than laboratory measurements of the Chang'E-5 lunar regolith samples. The reason for this may be related to uncertainty in the empirical formula from Fa and Wieczorek [57].

The  $\text{FeO}$  and  $\text{TiO}_2$  contents of the lunar regolith obtained by the Visible and Near-Infrared Imaging Spectrometer (VNIS) onboard the Chang'E-3 Yutu rover are  $\sim 22.8$  wt.% and  $\sim 5$  wt.%, respectively (Ling et al. [58]). This indicates that the  $\text{FeO}$  and  $\text{TiO}_2$  contents in the lunar regolith at the Chang'E-3 and Chang'E-5 landing sites are almost the same (Tian et al. [56], Ling et al. [58]). Similarly, the  $\text{FeO}$  and  $\text{TiO}_2$  contents of the lunar regolith obtained by the VNIS onboard the Chang'E-4 Yutu-2 rover are 7.42–18.82 wt.% and  $\sim 1.48$ –2.1 wt.%, respectively (Zeng et al. [59]), and the loss tangent of the lunar regolith retrieved by the Yutu-2 radar is  $\sim 0.005$  (Li et al. [8]), which is close to that of typical lunar regolith (McKay et al. [21]).

In terms of  $\text{TiO}_2+\text{FeO}$  content, it is high in the lunar regolith at the Chang'E-3 and Chang'E-5 landing sites and small at the Chang'E-4 site. One possible reason for this is related to past volcanic eruptions on the Moon. Historically, the Moon has experi-

enced at least two major volcanic eruptions. According to basalt samples returned by the Apollo and Luna missions, the first peak of volcanic activity on the Moon was between 3.1 Ga and  $\sim 4.3$  Ga (Morota et al. [60]), while the second peak of volcanic activity was  $\sim 1.8$  Ga to 2.5 Ga (Morota et al. [60], Haruyama et al. [61]). The mare basalt at the Chang'E-4 landing area has an age of  $\sim 3.6$ – $3.7$  Ga (Chang et al. [49], Huang et al. [50], Xiao et al. [52]), which probably formed during the period of the first peak of volcanic activity. The geological ages of the Chang'E-3 and Chang'E-5 landing sites are  $\sim 2.5$  Ga and 2.0 Ga (Li et al. [28], Xiao et al. [40]), respectively, and the mare basalt units at these sites probably formed during the second peak of volcanic activity. The mare basalt is formed from cooled volcanic magma which contains lunar mineral materials (e.g., ilmenite), and is the source of the  $\text{TiO}_2 + \text{FeO}$  content in the lunar regolith. The lunar regolith is a layer of loose materials covering the bedrock, and was predominantly formed by weathering processes (e.g., impact events) in the local mare basalt (McKay et al. [21]). The  $\text{TiO}_2 + \text{FeO}$  content in the lunar regolith at the Chang'E-3 and Chang'E-5 landing sites is quite different from that at the Chang'E-4 site, which may be due to the weathering time of the Chang'E-4 regolith being longer, although the mechanism of the decreased  $\text{TiO}_2 + \text{FeO}$  content in the lunar regolith with weathering time remains unknown and requires further study. In addition, most of the lunar regolith at the Chang'E-4 landing area is not mainly weathered by the local basalt materials, instead being dominated by foreign ejecta materials (e.g., Orientale basin, Finsen crater, etc.), which may be the reason for the low  $\text{TiO}_2 + \text{FeO}$  content of the lunar regolith in this area.

In terms of the loss tangent, that of the Chang'E-5 regolith is greater than that of the Chang'E-3, although the  $\text{TiO}_2 + \text{FeO}$  content at these two landing areas is almost the same. One possible reason for this is that the older lunar surface age decreases the loss tangent of the lunar regolith. This may not be related to the  $\text{TiO}_2 + \text{FeO}$  content; one possible factor is that the particle size of the lunar regolith grows gradually finer and its interior heterogeneity becomes more aggregated with age (Ding et al. [54]). Another possible factor is that the frequency of the Chang'E-5 radar is higher than that of the Chang'E-3 radar; when observing the same medium at a different frequency, the loss tangent measured by the higher frequency radar is likely to be larger than that of the lower-frequency radar.

The loss tangents of the Chang'E-3 regolith ( $\sim 0.0124$ ) and the Chang'E-5 regolith ( $\sim 0.0148$ ) are larger than that of typical Apollo lunar regolith samples, which is  $\sim 0.005$  (McKay et al. [21]), and even reach that of dense basalt, which is usually larger than  $10^{-3}$  (McKay et al. [21]). Apollo and Luna missions samples were almost always collected from older geological units (3.1 Ga to  $\sim 4.3$  Ga) on the Moon, while the geological ages of the Chang'E-5 and the Chang'E-3 landing areas are younger (2.0 Ga and  $\sim 2.5$  Ga). Therefore, we suggest that a loss tangent of the lunar regolith larger than  $10^{-3}$  is reasonable.

#### 4.4. Indications for Subsequent Radar Observations of the Moon

Radars with different working systems, different frequencies, and different observation modes will or have been involved in Lunar observation (Ding et al. [1], Zou et al. [62], Long et al. [63]). The loss tangent value directly affects the penetration depth of radar observation of the Moon (Xing et al. [11], Ding et al. [22]). In this paper, the relationship between the geological age of the lunar surface and the loss tangent is fitted; the applicability of the empirical formula can cover almost all the mare regions, which make up 17% the Moon's area (Head III [64]). As long as the geological age of the observation area is known, the loss tangent in the lunar regolith can be preliminarily calculated, which can provide parametric support for full interpretation of radar observation data (Li et al. [8], Ding et al. [22]). For in situ radars (e.g., the Chang'E-4 radar), the loss tangent estimated by the radar echo signal can be used to reverse the variations in the geological age of a mare unit within a small range. However, the empirical fitting formula used in this paper has only three observations, and as such the applicability and universality of the formula need to be improved via additional observation data.

## 5. Conclusions

The LRPR carried by Chang'E-5 provides an unprecedented opportunity to observe the interior structure of the lunar regolith and retrieve its dielectric properties. The Chang'E-5 landing site is located on the youngest basalt unit, which is characterized by the high loss tangent of its regolith layer. The loss tangent within  $\sim 2.8$  m of the lunar regolith is estimated to be  $0.0148 \pm 0.0016$  using the frequency shift method, and the corresponding  $\text{TiO}_2 + \text{FeO}$  content is constrained to be  $28.21 \pm 1.57\%$ . The results obtained from the in situ Chang'E-5 LRPR data have been subjected to a comparative analysis with those of the Chang'E-3 and Chang'E-4 landing sites and found to be consistent with laboratory measurements of Apollo regolith samples. Integrated analysis of the results from the three Chang'E missions reconfirm a negative relationship between the loss tangent and the geological age of the lunar surface. When the geologic age of the mare unit is older, the loss tangent of the lunar regolith is smaller and the penetrating ability of radar waves is stronger. Furthermore, the empirical formula obtained in this paper may be applicable to other airless planetary bodies.

In addition, the frequency shift method is a simple, effective, and widely used approach for calculating the loss tangent of the lunar regolith. In the future, the full wave inversion method can be considered to retrieve the dielectric properties (e.g., the relative permittivity and the loss tangent) of the lunar regolith using the LRPR data at the Chang'E-5 landing site. The full wave inversion method may be able to obtain a finer distribution of dielectric properties (Lavoué et al. [65]), especially for the interpretation of the interior structure of the lunar regolith, which could be very helpful.

**Author Contributions:** Conceptualization, C.D., S.H.; methodology, C.D.; software, C.D. and Y.S.; validation, C.D., Z.L., Z.Z., M.S., Q.L., Y.S. and S.H.; formal analysis, C.D.; investigation, C.D.; resources, C.D.; data curation, C.D., Z.Z., R.W., Z.L. and Y.L.; writing—original draft preparation, C.D.; writing—review and editing, C.D., Q.L., Y.S., C.L. and S.H.; visualization, C.D.; project administration, C.D., Q.L., C.L. and S.H.; funding acquisition, C.D. and S.H. All authors have read and agreed to the published version of the manuscript.

**Funding:** This work is supported by the National Natural Science Foundation of China (Grant No. 42004099), the Opening Fund of the Key Laboratory of Lunar and Deep Space Exploration, Chinese Academy of Sciences (No. LDSE202005), the Young Teachers Startup Fund of Shenzhen University (Grant No. 860-000002112127), the Fund of Shanghai Institute of Aerospace System Engineering (No. PZ\_YY\_SYF\_JY200275), and the Shenzhen Municipal Government Investment Project (No. 2106-440300-04-03-901272).

**Data Availability Statement:** The LRPR data used in this study can be download from the website (<http://www.dx.doi.org/10.12350/CLPDS.GRAS.CE5.LRPR-01.vA>, accessed on 2 August 2022).

**Acknowledgments:** We thank the Ground Application System of Lunar Exploration, National Astronomical Observatories, Chinese Academy of Sciences for providing the data used in this study. Comments and suggestions from all anonymous reviewers have improved the quality of the paper.

**Conflicts of Interest:** The authors declare no conflict of interest.

## References

1. Ding, C.; Jianqing, F.; Lei, Z. A review of application of radar-detection techniques in lunar exploration. *Astron. Res. Technol.* **2015**, *12*, 228–242.
2. Li, C.; Liu, J.; Zuo, W.; Su, Y.; Ouyang, Z. Progress of China's Lunar Exploration (2011–2020). *J. Space Sci.* **2021**, *41*, 68–75. [[CrossRef](#)]
3. Hörz, F.; Grieve, R.; Heiken, G.; Spudis, P.; Binder, A. Lunar surface processes. In *Lunar Source Book: A User's Guide to the Moon*; Cambridge University Press: Cambridge, UK, 1991; pp. 61–120.
4. Carrier, W.D.; Olhoeft, G.R.; Mendell, W. Physical properties of the lunar surface. In *Lunar Source Book: A User's Guide to the Moon*; Cambridge University Press: Cambridge, UK, 1991; pp. 475–594.
5. Campbell, M.J.; Ulrichs, J. Electrical properties of rocks and their significance for lunar radar observations. *J. Geophys. Res.* **1969**, *74*, 5867–5881. [[CrossRef](#)]

6. Feng, J.; Su, Y.; Ding, C.; Xing, S.; Dai, S.; Zou, Y. Dielectric properties estimation of the lunar regolith at CE-3 landing site using lunar penetrating radar data. *Icarus* **2017**, *284*, 424–430. [[CrossRef](#)]
7. Ding, C.; Xiao, Z.; Su, Y.; Cui, J. Hyperbolic reflectors determined from peak echoes of ground penetrating radar. *Icarus* **2021**, *358*, 114280. [[CrossRef](#)]
8. Li, C.; Su, Y.; Pettinelli, E.; Xing, S.; Ding, C.; Liu, J.; Ren, X.; Lauro, S.E.; Soldovieri, F.; Zeng, X. The Moon's farside shallow subsurface structure unveiled by Chang'E-4 Lunar Penetrating Radar. *Sci. Adv.* **2020**, *6*, eaay6898. [[CrossRef](#)]
9. Ding, C.; Xiao, Z.; Wu, B.; Li, Z.; Su, Y.; Zhou, B.; Liu, K.; Cui, J. Rock Fragments in Shallow Lunar Regolith: Constraints by the Lunar Penetrating Radar Onboard the Chang'E-4 Mission. *J. Geophys. Res. Planets* **2021**, *126*, e2021JE006917. [[CrossRef](#)]
10. Pommerol, A.; Kofman, W.; Audouard, J.; Grima, C.; Beck, P.; Mouginot, J.; Herique, A.; Kumamoto, A.; Kobayashi, T.; Ono, T. Detectability of subsurface interfaces in lunar maria by the LRS/SELENE sounding radar: Influence of mineralogical composition. *Geophys. Res. Lett.* **2010**, *37*. [[CrossRef](#)]
11. Xing, S.G.; Su, Y.; Feng, J.Q.; Dai, S.; Xiao, Y.; Ding, C.Y.; Li, C.L. The penetrating depth analysis of Lunar Penetrating Radar onboard Chang'E-3 rover. *Res. Astron. Astrophys.* **2017**, *17*, 46. [[CrossRef](#)]
12. Hillier, J.K.; Buratti, B.J.; Hill, K. Multispectral photometry of the moon and absolute calibration of the clementine UV/Vis camera. *Icarus* **1999**, *141*, 205–225. [[CrossRef](#)]
13. Sato, H.; Robinson, M.S.; Lawrence, S.J.; Denevi, B.W.; Hapke, B.; Jolliff, B.L.; Hiesinger, H. Lunar mare TiO<sub>2</sub> abundances estimated from UV/Vis reflectance. *Icarus* **2017**, *296*, 216–238. [[CrossRef](#)]
14. Fang, G.Y.; Zhou, B.; Ji, Y.C.; Zhang, Q.Y.; Shen, S.X.; Li, Y.X.; Guan, H.F.; Tang, C.J.; Gao, Y.Z.; Lu, W.; et al. Lunar Penetrating Radar onboard the Chang'E-3 mission. *Res. Astron. Astrophys.* **2014**, *14*, 1607–1622. [[CrossRef](#)]
15. Su, Y.; Fang, G.Y.; Feng, J.Q.; Xing, S.G.; Ji, Y.C.; Zhou, B.; Gao, Y.Z.; Li, H.; Dai, S.; Xiao, Y.; et al. Data processing and initial results of Chang'E-3 lunar penetrating radar. *Res. Astron. Astrophys.* **2014**, *14*, 1623–1632. [[CrossRef](#)]
16. Xiao, Y.; Su, Y.; Dai, S.; Feng, J.; Xing, S.; Ding, C.; Li, C. Ground experiments of Chang'E-5 lunar regolith penetrating radar. *Adv. Space Res.* **2019**, *63*, 3404–3419. [[CrossRef](#)]
17. Zhou, H.; Feng, X.; Ding, C.; Dong, Z.; Liu, C.; Zhang, Y.; Meng, Z. Yutu-2 radar sounding evidence of a buried crater at Chang'E-4 landing site. *IEEE Trans. Geosci. Remote Sens.* **2021**, *60*, 1–19. [[CrossRef](#)]
18. Wang, R.; Su, Y.; Ding, C.; Dai, S.; Liu, C.; Zhang, Z.; Hong, T.; Zhang, Q.; Li, C. A Novel Approach for Permittivity Estimation of Lunar Regolith Using the Lunar Penetrating Radar Onboard Chang'E-4 Rover. *Remote Sens.* **2021**, *13*, 3679. [[CrossRef](#)]
19. Ulaby, F.T.; Long, D.G.; Blackwell, W.J.; Elachi, C.; Fung, A.K.; Ruf, C.; Sarabandi, K.; Zebker, H.A.; Van Zyl, J. *Microwave Radar and Radiometric Remote Sensing*; University of Michigan Press: Ann Arbor, MI, USA, 2014; Volume 4.
20. Orosei, R.; Rossi, A.P.; Cantini, F.; Caprarelli, G.; Carter, L.M.; Papiano, I.; Cartacci, M.; Cicchetti, A.; Noschese, R. Radar sounding of Lucus Planum, Mars, by MARSIS. *J. Geophys. Res. Planets* **2017**, *122*, 1405–1418. [[CrossRef](#)]
21. McKay, D.S.; Heiken, G.; Basu, A.; Blanford, G.; Simon, S.; Reedy, R.; French, B.M.; Papike, J. The lunar regolith. In *Lunar Source Book: A User's Guide to the Moon*; Cambridge University Press: Cambridge, UK, 1991; pp. 285–356.
22. Ding, C.; Xiao, Z.; Su, Y.; Zhao, J.; Cui, J. Compositional variations along the route of Chang'E-3 Yutu rover revealed by the lunar penetrating radar. *Prog. Earth Planet. Sci.* **2020**, *7*, 1–11. [[CrossRef](#)]
23. Strangway, D.; Pearce, G.; Olhoeft, G. Magnetic and dielectric properties of lunar samples. In *Sov.-Amer. Conf. Cosmochem. Moon Planets*. pp. 417–431.
24. Liu, L.; Lane, J.W.; Quan, Y. Radar attenuation tomography using the centroid frequency downshift method. *J. Appl. Geophys.* **1998**, *40*, 105–116. [[CrossRef](#)]
25. Irving, J.D.; Knight, R.J. Removal of wavelet dispersion from ground-penetrating radar data. *Geophysics* **2003**, *68*, 960–970. [[CrossRef](#)]
26. Li, C.; Hu, H.; Yang, M.F.; Pei, Z.Y.; Zhou, Q.; Ren, X.; Liu, B.; Liu, D.; Zeng, X.; Zhang, G. Characteristics of the lunar samples returned by the Chang'E-5 mission. *Natl. Sci. Rev.* **2022**, *9*, nwab188. [[CrossRef](#)]
27. Qiao, L.; Chen, J.; Xu, L.; Wan, S.; Cao, H.; Li, B.; Ling, Z. Geology of the Chang'E-5 landing site: Constraints on the sources of samples returned from a young nearside mare. *Icarus* **2021**, *364*, 114480. [[CrossRef](#)]
28. Li, Q.L.; Zhou, Q.; Liu, Y.; Xiao, Z.; Lin, Y.; Li, J.H.; Ma, H.X.; Tang, G.Q.; Guo, S.; Tang, X.; et al. Two-billion-year-old volcanism on the Moon from Chang'E-5 basalts. *Nature* **2021**, *600*, 54–58. [[CrossRef](#)]
29. Che, X.; Nemchin, A.; Liu, D.; Long, T.; Wang, C.; Norman, M.D.; Joy, K.H.; Tartese, R.; Head, J.; Jolliff, B.; et al. Age and composition of young basalts on the Moon, measured from samples returned by Chang'E-5. *Science* **2021**, *374*, 887–890. [[CrossRef](#)]
30. Wu, B.; Huang, J.; Li, Y.; Wang, Y.; Peng, J. Rock abundance and crater density in the candidate Chang'E-5 landing region on the Moon. *J. Geophys. Res. Planets* **2018**, *123*, 3256–3272. [[CrossRef](#)]
31. Su, Y.; Wang, R.; Deng, X.; Zhang, Z.; Zhou, J.; Xiao, Z.; Ding, C.; Li, Y.; Dai, S.; Ren, X.; et al. Hyperfine Structure of Regolith Unveiled by Chang'E-5 Lunar Regolith Penetrating Radar. *IEEE Trans. Geosci. Remote Sens.* **2022**, *60*, 1–14. [[CrossRef](#)]
32. Qian, Y.; Xiao, L.; Wang, Q.; Head, J.W.; Yang, R.; Kang, Y.; van der Bogert, C.H.; Hiesinger, H.; Lai, X.; Wang, G.; et al. China's Chang'E-5 landing site: Geology, stratigraphy, and provenance of materials. *Earth Planet. Sci. Lett.* **2021**, *561*, 116855. [[CrossRef](#)]
33. McGetchin, T.R.; Settle, M.; Head, J. Radial thickness variation in impact crater ejecta: Implications for lunar basin deposits. *Earth Planet. Sci. Lett.* **1973**, *20*, 226–236. [[CrossRef](#)]
34. Pike, R.J. Depth/diameter relations of fresh lunar craters: Revision from spacecraft data. *Geophys. Res. Lett.* **1974**, *1*, 291–294. [[CrossRef](#)]

35. Feng, J.; Siegler, M.A.; White, M.N. Shallow Regolith Structure and Obstructions Detected by Lunar Regolith Penetrating Radar at Chang'E-5 Drilling Site. *Remote Sens.* **2022**, *14*, 3378. [[CrossRef](#)]
36. Li, Y.; Lu, W.; Fang, G.; Zhou, B.; Shen, S. Performance verification of lunar regolith penetrating array radar of Chang'E-5 mission. *Adv. Space Res.* **2019**, *63*, 2267–2278. [[CrossRef](#)]
37. Feng, J.Q.; Su, Y.; Li, C.L.; Dai, S.; Xing, S.G.; Xiao, Y. An imaging method for Chang'E-5 Lunar Regolith Penetrating Radar. *Planet. Space Sci.* **2019**, *167*, 9–16. [[CrossRef](#)]
38. Quan, Y.; Harris, J.M. Seismic attenuation tomography using the frequency shift method. *Geophysics* **1997**, *62*, 895–905. [[CrossRef](#)]
39. Lauro, S.E.; Mattei, E.; Cosciotti, B.; Di Paolo, F.; Arcone, S.A.; Viccaro, M.; Pettinelli, E. Electromagnetic signal penetration in a planetary soil simulant: Estimated attenuation rates using GPR and TDR in volcanic deposits on Mount Etna. *J. Geophys. Res.-Planets* **2017**, *122*, 1392–1404. [[CrossRef](#)]
40. Xiao, L.; Zhu, P.; Fang, G.; Xiao, Z.; Zou, Y.; Zhao, J.; Zhao, N.; Yuan, Y.; Qiao, L.; Zhang, X. A young multilayered terrane of the northern Mare Imbrium revealed by Chang'E-3 mission. *Science* **2015**, *347*, 1226–1229. [[CrossRef](#)] [[PubMed](#)]
41. Qiao, L.; Xiao, Z.Y.; Zhao, J.N.; Xiao, L. Subsurface structures at the Chang'E-3 landing site: Interpretations from orbital and in-situ imagery data. *J. Earth Sci.* **2016**, *27*, 707–715. [[CrossRef](#)]
42. Melosh, H.J. *Impact Cratering: A Geologic Process*; Research Supported by NASA; Oxford 511 Monographs on Geology and Geophysics, No. 11; Oxford University Press: New York, NY, USA, 1989; Volume 11, 253p.
43. Taylor, G.J.; Keil, K.; Warner, R.D. Petrology of Apollo 17 deep drill core. I-Depositional history based on modal analyses of 70009, 70008, and 70007. *Lunar Planet. Sci. Conf. Proc.* **1977**, *8*, 3195–3222.
44. Stöffler, D.; Gault, D.E.; Wedekind, J.; Polkowski, G. Experimental hypervelocity impact into quartz sand: Distribution and shock metamorphism of ejecta. *J. Geophys. Res. (1896–1977)* **1975**, *80*, 4062–4077. [[CrossRef](#)]
45. Fa, W.Z.; Liu, T.T.; Zhu, M.H.; Haruyama, J. Regolith thickness over Sinus Iridum: Results from morphology and size-frequency distribution of small impact craters. *J. Geophys. Res.-Planets* **2014**, *119*, 1914–1935. [[CrossRef](#)]
46. Ding, C.; Li, C.; Xiao, Z.; Su, Y.; Xing, S.; Wang, Y.; Feng, J.; Dai, S.; Xiao, Y.; Yao, M. Layering Structures in the Porous Material Beneath the Chang'E-3 Landing Site. *Earth Space Sci.* **2020**, *7*, e2019EA000862. [[CrossRef](#)]
47. Fa, W.; Zhu, M.H.; Liu, T.T.; Plescia, J.B. Regolith stratigraphy at the Chang'E-3 landing site as seen by lunar penetrating radar. *Geophys. Res. Lett.* **2015**, *42*, 10179–10187. [[CrossRef](#)]
48. Sharpton, V.L. Outcrops on lunar crater rims: Implications for rim construction mechanisms, ejecta volumes and excavation depths. *J. Geophys. Res. Planets* **2014**, *119*, 154–168. [[CrossRef](#)]
49. Chang, Y.; Xiao, Z.; Wang, Y.; Ding, C.; Cui, J.; Cai, Y. An Updated Constraint on the local stratigraphy at the Chang'E-4 landing site. *Earth Planet. Phys.* **2021**, *5*, 19–31. [[CrossRef](#)]
50. Huang, J.; Xiao, Z.; Flahaut, J.; Martinot, M.; Head, J.; Xiao, X.; Xie, M.; Xiao, L. Geological characteristics of Von Kármán crater, northwestern south pole-Aitken Basin: Chang'E-4 landing site region. *J. Geophys. Res. Planets* **2018**, *123*, 1684–1700. [[CrossRef](#)]
51. Pasckert, J.H.; Hiesinger, H.; van der Bogert, C.H. Lunar farside volcanism in and around the South Pole–Aitken basin. *Icarus* **2018**, *299*, 538–562. [[CrossRef](#)]
52. Xiao, Z.; Ding, C.; Xie, M.; Cai, Y.; Cui, J.; Zhang, K.; Wang, J. Ejecta From the Orientale Basin at the Chang'E-4 Landing Site. *Geophys. Res. Lett.* **2021**, *48*, e2020GL090935. [[CrossRef](#)]
53. Boivin, A.; Tsai, C.A.; Hickson, D.; Ghent, R.; Daly, M. Preliminary Broadband Measurements of Dielectric Permittivity of Planetary Regolith Analog Materials Using a Coaxial Transmission Line. In Proceedings of the 46th Lunar and Planetary Science Conference, the Woodlands, TX, USA, 16–20 March 2015; p. 2487.
54. Ding, C.; Xiong, S.; Li, J.; Su, Y.; Huang, S. Yutu-2 radar observation of the lunar regolith heterogeneity at the Chang'E-4 landing site. *Astron. Astrophys.* **2022**, *664*, A43. [[CrossRef](#)]
55. Lemelin, M.; Lucey, P.G.; Song, E.; Taylor, G.J. Lunar central peak mineralogy and iron content using the Kaguya Multiband Imager: Reassessment of the compositional structure of the lunar crust. *J. Geophys. Res. Planets* **2015**, *120*, 869–887. [[CrossRef](#)]
56. Tian, H.C.; Wang, H.; Chen, Y.; Yang, W.; Zhou, Q.; Zhang, C.; Lin, H.L.; Huang, C.; Wu, S.T.; Jia, L.H.; et al. Non-KREEP origin for Chang'E-5 basalts in the Procellarum KREEP Terrane. *Nature* **2021**, *600*, 59–63. [[CrossRef](#)]
57. Fa, W.; Wieczorek, M.A. Regolith thickness over the lunar nearside: Results from Earth-based 70-cm Arecibo radar observations. *Icarus* **2012**, *218*, 771–787. [[CrossRef](#)]
58. Ling, Z.; Jolliff, B.L.; Wang, A.; Li, C.; Liu, J.; Zhang, J.; Li, B.; Sun, L.; Chen, J.; Xiao, L.; et al. Correlated compositional and mineralogical investigations at the Chang'E-3 landing site. *Nat. Commun.* **2015**, *6*, 8880. [[CrossRef](#)]
59. Zeng, Q.; Chen, S.; Zhang, Y.; Mu, Y.; Dai, R.; Yang, C.; Li, A.; Lu, P. Mineralogical and chemical properties inversed from 21-lunar-day VNIS observations taken during the Chang'E-4 mission. *Sci. Rep.* **2021**, *11*, 15435. [[CrossRef](#)]
60. Morota, T.; Haruyama, J.; Ohtake, M.; Matsunaga, T.; Honda, C.; Yokota, Y.; Kimura, J.; Ogawa, Y.; Hirata, N.; Demura, H.; et al. Timing and characteristics of the latest mare eruption on the Moon. *Earth Planet. Sci. Lett.* **2011**, *302*, 255–266. [[CrossRef](#)]
61. Haruyama, J.; Ohtake, M.; Matsunaga, T.; Morota, T.; Honda, C.; Yokota, Y.; Abe, M.; Ogawa, Y.; Miyamoto, H.; Iwasaki, A.; et al. Long-lived volcanism on the lunar farside revealed by SELENE Terrain Camera. *Science* **2009**, *323*, 905–908. [[CrossRef](#)]
62. Zou, Y.; Liu, Y.; Jia, Y. Overview of China's Upcoming Chang'E Series and the Scientific Objectives and Payloads for Chang'E 7 Mission. In Proceedings of the 51th Lunar and Planetary Science Conference, the Woodlands, TX, USA, 18–22 March 2019; p. 1755.

63. Long, T.; Zeng, T.; Hu, C.; Dong, X.; Chen, L.; Liu, Q.; Xie, Y.; Ding, Z.; Li, Y.; Wang, Y.; et al. High resolution radar real-time signal and information processing. *China Commun.* **2019**, *16*, 105–133.
64. Head, J.W., III. Lunar volcanism in space and time. *Rev. Geophys.* **1976**, *14*, 265–300. [[CrossRef](#)]
65. Lavoué, F.; Brossier, R.; Métivier, L.; Garambois, S.; Virieux, J. Two-dimensional permittivity and conductivity imaging by full waveform inversion of multioffset GPR data: A frequency-domain quasi-Newton approach. *Geophys. J. Int.* **2014**, *197*, 248–268. [[CrossRef](#)]